



Heat release rate surrogate for ammonia–hydrogen premixed flames under various conditions

Jiangkuan Xing^{*}, Abhishek Lakshman Pillai, Ryoichi Kurose

Department of Mechanical Engineering and Science, Kyoto University, Kyoto daigaku-Katsura, Nishikyo-ku, Kyoto 615-8540, Japan

ARTICLE INFO

Keywords:

Ammonia
Hydrogen
Heat release rate surrogates
Premixed flame

ABSTRACT

Blending hydrogen has proven an efficient method to enhance the combustion stability of gaseous ammonia flames. Heat release rate (HRR), as an important parameter to indicate combustion process, is hard to be directly measured and highly dependent on the fuel components, equivalence ratios, and operation conditions. This paper presents a comprehensive study on developing a general HRR surrogate (HRRS) for ammonia–hydrogen premixed flames under various conditions. Firstly, reaction mechanisms for ammonia/hydrogen premixed combustion are evaluated under various conditions, by comparing the predicted laminar flame speeds with the experimental data collected from published literature. The reaction mechanism developed by Shrestha et al., (2021) performs the best under various conditions. Then, series of one-dimensional freely propagating premixed flames under various conditions are calculated using this reaction mechanism and analyzed to explore the effects of blending ratios, pre-heat temperatures, equivalence ratios, and pressures on the HRR reconstruction for ammonia–hydrogen premixed flames from the viewpoint of chemical kinetics, and also serve as a database for the identification of HRRSs. It is found that equivalence ratio and blending ratio have significant effects on the HRR reconstruction, while the effects of pressure and initial temperature are relatively limited. Subsequently, the general HRRS, $[\text{NH}_2]^{1.53}[\text{OH}]^{0.28}$, is identified for ammonia–hydrogen premixed flames under various conditions using a grid-search optimization method. Finally, the general HRRS is further comprehensively validated on several 2D and 3D turbulent premixed flames of ammonia–hydrogen under various conditions. The comparisons with the two previous HRRSs also demonstrate that the present developed HRRS is superior and more stable temporally.

1. Introduction

Ammonia, as a carbon-free fuel and hydrogen carrier, is regarded as an attractive alternative for energy and combustion systems [1]. However, its relatively low flame speed brings a challenge to the stable combustion of pure ammonia gaseous flame [2]. Efforts have been made to address this issue. A high-intensity swirl flow was found to help create the re-circulation region, facilitate the transfer of heat and reactive radicals, and further stabilize the ammonia gaseous flame [3]. In the fuel side, co-firing with small-molecule active fuels, such as methane or hydrogen, is proven able to enhance the combustion stability [4–7]. In the oxidizer side, oxygen-enriched technology can also enhance the laminar flame speed of ammonia combustion [8–11]. In addition, pre-heating oxidizer or fuel/oxidizer mixture is also an alternative to enhance ammonia combustion [12,13]. Those methods involve complicated treatments of different local equivalence ratios, blending ratios (BRs), pressures and pre-heat temperatures. Well understanding the flame characteristics under various conditions are of

great significance for developing stable, clean, and efficient ammonia combustion technologies.

Heat release rate (HRR), as one of the important properties of flame characteristics, is useful to identify the flame regions and indicates important physical process [14]. However, its quantitative measurement involves accurate measurements of temperature and species concentrations simultaneously, which is very challenging and remains to be currently impractical to be conducted [15]. Instead, chemical quantities or scalars that have strong correlations with the actual HRR field and can be measured through optical techniques such as fluorescence and chemiluminescence are alternatively thought as the HRR surrogates (HRRSs) [16]. For the chemiluminescence method, the relation between the excited species and the ground state needs to be defined [17,18]. For the exploration of suitable HRRSs for flames, methane/air flame has received the most attention [19–22], and HRRSs for other fuels, such as syngas [23] and hydrogen [24], have also been explored. Gazi et al. [25] explored the suitability of HRRSs

^{*} Corresponding author.

E-mail address: xing.jiangkuan.6h@kyoto-u.ac.jp (J. Xing).

Nomenclature

BR	Blending ratio, [-]
HRRS	Heat release rate surrogate
DNS	Direct numerical simulation
T_u	Unburnt temperature, [K]
S_L	Laminar flame speed, [cm/s]
P	Pressure, [bar]
$RMSE$	Root mean square error, [cm/s]
U_j	Velocity, [m/s]
$U_{central}$	Velocity of the central flow, [m/s]
$Z(v)$	Reconstruction error of v variable, [-]
\dot{Q}	Heat release rate term, [W/m ³]
t	Time, [s]
N_i	Sample number of i variable, [-]
f	mean error score, [-]
\dot{Q}^+	Normalized \dot{Q} , [-]
X_i^+	Normalized mole fraction of species i , [-]
T_{fresh}	Unburnt temperature, [K]
κ	Flame curvature, [1/m]
HRR	Heat release rate, [W/m ³]
1D	One dimensional
2D	Two dimensional
3D	Three dimensional
ϕ	Equivalence ratio, [-]
R^2	Correlation coefficient, [-]
H	Jet width, [m]
L_x	Domain length, [m]
U_{pilot}	Velocity of the pilot flow, [m/s]
v	Selected variables
x, y, z	Location, [m]
t_j	One flow period, [s]
p, q	Component values, [-]
$[A],[B]$	Species mole fraction, [-]
$\dot{\omega}_r^+$	Normalized reaction rate, [-]
τ^*	Normalized time period, [-]
T_{burnt}	Burnt temperature, [K]

previously developed for methane to other fuels, including ethanol, benzene, acetylene, and other hydrocarbon fuels, under various equivalence ratios. They found that the optimal HRRS is strongly dependent on the fuel types and equivalence ratios. For the multi-component fuel flames, Nikolaou and Swaminathan [20] found that the reaction rate of $\text{OH}+\text{CH}_2\text{O}\rightleftharpoons\text{HCO}+\text{H}_2\text{O}$ worked well for methane/air flame but was inadequate for multi-component fuel flames. As for ammonia flames, only a few works have been reported for determining the optimal HRRS. For pure ammonia flames, Cheng et al. [26] proposed three HRR surrogates from series of one-dimensional (1D) premixed flames and found that their performances varied with equivalence ratios and pressures. They further updated the optimal HRRSs by considering various temperatures, pressures, and equivalence ratios, and validated their performances using three-dimensional (3D) direct numerical simulation (DNS) data of turbulent premixed ammonia/air flames [27]. Zhu et al. [28] analyzed the heat release characteristics of ammonia-methane combustion from 1D freely propagating premixed flames, and found that product $[\text{OH}][\text{CH}_2\text{O}]$ can well reproduce HRR under various conditions. Recently, Chi et al. [29] identified two HRRSs for ammonia-hydrogen premixed flames using a data-driven physics-informed machine learning method, and validated their performances using 2D and 3D DNSs data. The heat release characteristics

of ammonia-hydrogen flames were also studied by Yang et al. [30] through DNS data of outwardly expanding turbulent premixed flames. It was found that NH_2 radical could be considered as a potential HRRS.

From the above discussions, the performances of HRRSs are strongly dependent on the fuel components (fuel species) and operation conditions (equivalence ratios, pressures, and pre-heated temperatures). In addition, as mentioned above, the practical combustion of ammonia needs some enhancement treatments, which may cover various equivalence ratios (two-stage combustion in the study of Ref. [12]), hydrogen BRs, pre-heated degrees, and pressures (atmospheric to engine/gas turbine conditions). The HRR characteristics of ammonia-hydrogen premixed flames under the above various conditions have not been fully understood, and the effects of equivalence ratios, BRs, preheated temperatures, and pressures need a more insightful exploration. Moreover, previous HRRSs for ammonia-hydrogen premixed flames were identified from limited conditions, and their validity under various conditions is unclear. There is still a lack of a general HRRS that can be used to accurately reconstruct the HRR field under various conditions.

Therefore, the present study aims to address the above issues. Firstly, reaction mechanisms for ammonia/hydrogen premixed combustion are evaluated under various BRs, pre-heat temperatures, equivalence ratios, and pressures through comparing with the available published experimental data. Then, series of one-dimensional freely propagating premixed flames under various conditions are calculated and analyzed to explore the effects of BRs, pre-heat temperatures, equivalence ratios, and pressures on the HRR reconstruction for ammonia-hydrogen premixed flames in the viewpoint of chemical kinetics, and also serve as a database for the identification of HRRS. Subsequently, the general HRRS for ammonia-hydrogen premixed flames for various conditions is identified using a grid-research optimization method. Finally, the identified HRRS is further comprehensively validated on several 2D and 3D turbulent premixed flames of ammonia-hydrogen under various conditions.

The rest of this paper is organized as follows. The evaluation of reaction mechanisms for ammonia-hydrogen premixed flames under various conditions are conducted in Section 2.1. The computational details and configurations used to construct the flame database for HRRS identification and validation are introduced from Sections 2.2 to 2.4. Section 3 presents the detailed approaches for identifying the general HRRS for various conditions. Section 4 validates the performance of the identified HRRS on the remaining 1D freely propagating premixed flames and 2D/3D-DNS results of turbulent premixed flames of ammonia-hydrogen. The last section provides the conclusion remarks.

2. Flame database construction

2.1. Evaluation of reaction mechanisms for ammonia-hydrogen flame

There have been considerable reaction mechanisms available for ammonia/hydrogen combustion chemistry, which have been partially validated using the experimental data under limited conditions obtained from their own experiments and/or from published literature. The present study aims to explore the HRR characteristics and identify a general HRRS for ammonia-hydrogen premixed flame under various preheat temperatures, pressures, BRs, and equivalence ratios. BR represents the mole fraction of hydrogen in the fuel stream. Therefore, before constructing the flame database, the available reaction mechanisms are firstly examined by comparing the predicted laminar flame speeds with the experimental data for various conditions. The experimental data of laminar flame speeds under various conditions are collected from studies of Han et al. [31], Ichikawa et al. [32], Kumar and Meyer [33], Lee et al. [34], Li et al. [35], and Shrestha et al. [10]. The reaction mechanisms developed by Dagaut et al. [36], Klippenstein et al. [37], Konnov et al. [38], Mathieu et al. [39], Nakamura et al. [40], Okafor et al. [41], Otomo et al. [42], Shrestha et al. [10,43], Stagni et al. [44], and Zhang et al. [45] are considered.

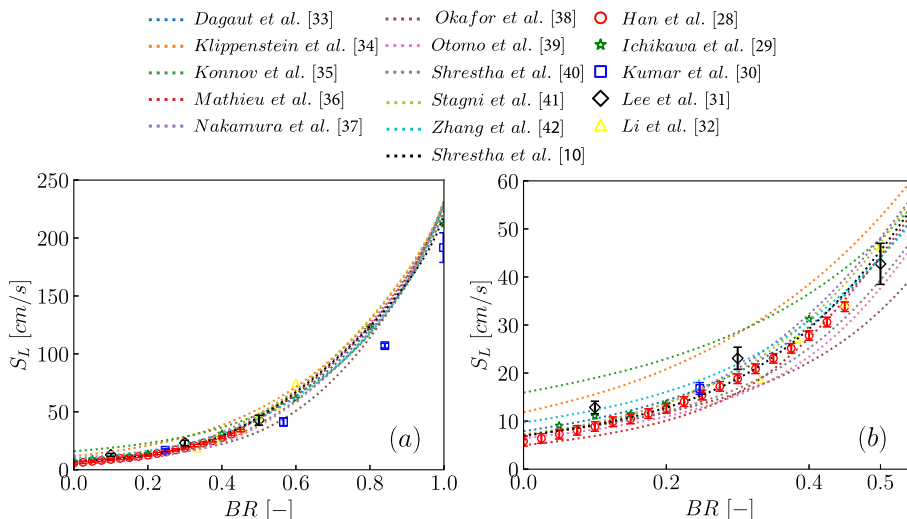


Fig. 1. Comparisons between the laminar flame speeds predicted with different reaction mechanisms (dash lines) and those measured in experiments (scatters) under different BRs ($P = 1$ bar, $T_u = 300$ K, and $\phi = 1.0$): (a) $BR = 0 - 1.0$; (b) $BR = 0 - 0.5$ (enlarged version of (a)).

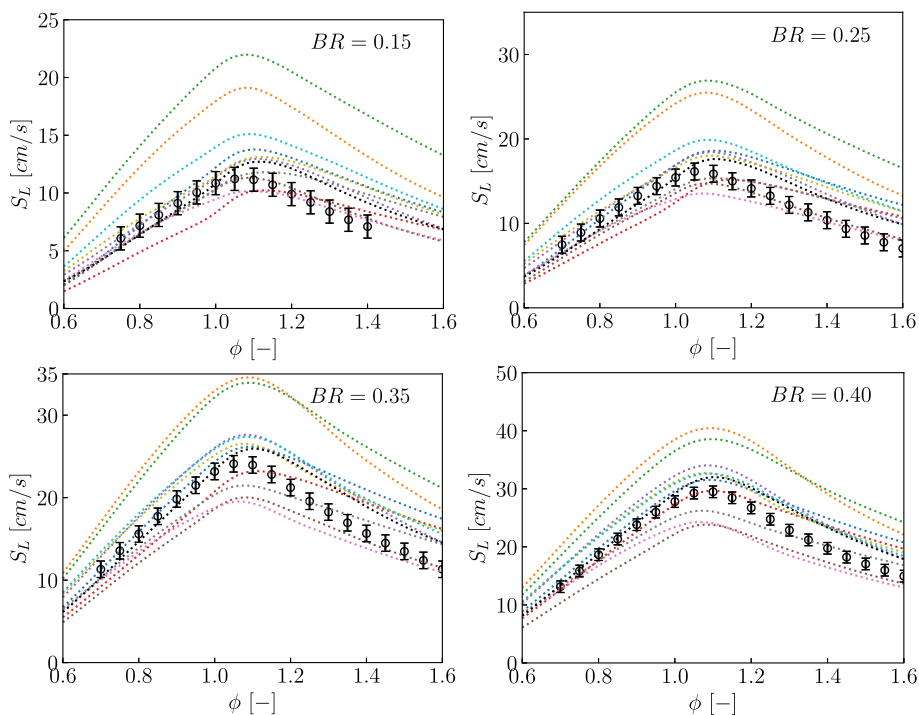


Fig. 2. Comparisons between the laminar flame speeds predicted with different reaction mechanisms (dash lines) and those measured in experiments (scatters) under different equivalence ratios and BRs ($P = 1$ bar). The line legend is same as that in Fig. 1, and the experimental data are collected from Han et al. [31].

Fig. 1 shows the comparisons of the laminar flame speeds under different BRs calculated ($P = 1$ bar, $T_u = 300$ K, and $\phi = 1.0$) with different mechanisms and measured in the experiments. The mechanisms, developed by Klippenstein et al., Konnov et al., and Zhang et al. overestimate the laminar flame speed under conditions of low hydrogen BRs. While the mechanisms developed by Okafor et al., Otomo et al., and Shrestha et al. can give good predictions under low BRs but underestimate the flame speeds under high BRs. The other mechanisms can well reproduce the experimental data. Especially, the reaction mechanism updated by Shrestha et al. [10] gave the best performance with the correlation coefficient $R^2 > 0.992$ and maximum root mean square error $RMSE < 4.2$ cm/s, while predictions of reaction

mechanisms developed by Klippenstein et al. and Konnov et al. have the $RMSE$ values larger than 10 cm/s.

Fig. 2 shows the comparisons under different equivalence ratios (0.6 – 1.6) and BRs (0.15, 0.25, 0.35, and 0.4). The mechanisms developed by Klippenstein et al., Konnov et al., Nakamura et al., Stagni et al., and Zhang et al. overestimate the laminar flame speeds under all the conditions, with negative R^2 values. Under the lean conditions, the mechanisms developed by Dagaut et al. and Shrestha et al. give the best predictions. Under the rich conditions, all mechanisms only can give acceptable predictions. Overall, reaction mechanisms developed by Shrestha et al. has the best performance with the $RMSE$ values

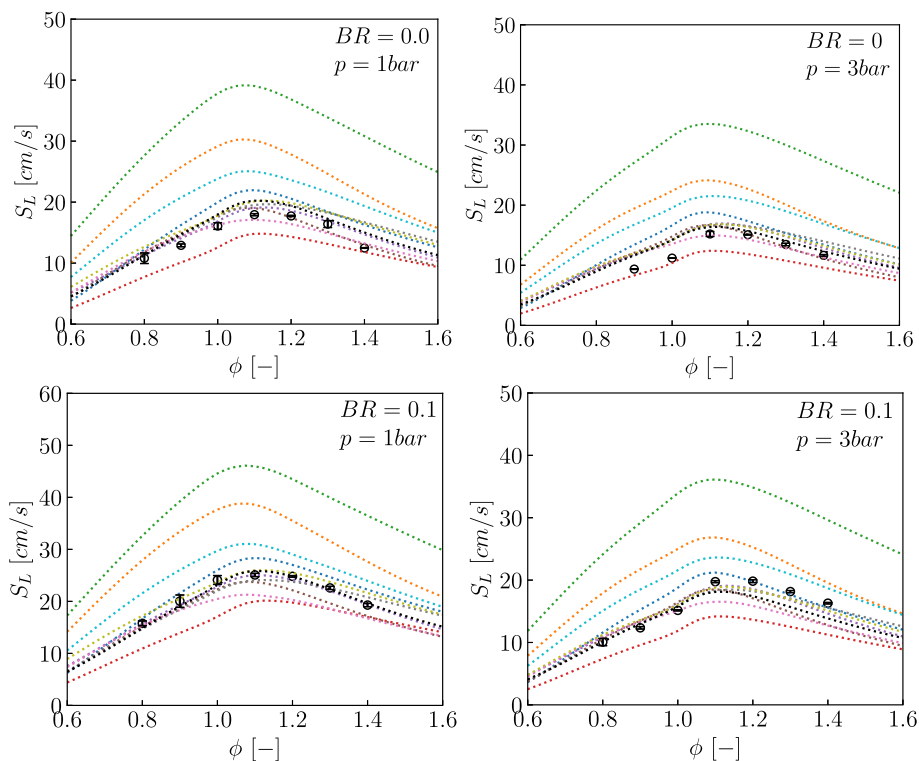


Fig. 3. Comparisons between the laminar flame speeds predicted with different reaction mechanisms (dash lines) and those measured in experiments (scatters) under different equivalence ratios, BRs and pressures ($T_{fresh} = 473$ K). The line legend is same as that in Fig. 1, and the experimental data are collected from Shrestha et al. [10].

less than 2.5 cm/s, while the reaction mechanism developed by Klippenstein et al. and Konnov et al. have the maximum *RMSE* values larger than 8 cm/s.

Figs. 3 and 4 shows the comparisons under different pre-heat temperatures, BRs, and pressures. For pure ammonia flame, the mechanisms developed by Otomo et al., Okafor et al., Shrestha et al., Nakamura et al., and Stagni et al. perform well with the *RMSE* values less than 2 cm/s. However, when the BR increases to 0.1, Okafor and Otomo mechanisms would significantly underestimate the laminar flame speeds under rich conditions, and the other mechanisms slightly underestimate those. The reaction mechanisms developed by Shrestha et al. has the best performance with the *RMSE* values less than 1.5 cm/s. Under high pressure conditions (5 bar and 7 bar), Otomo mechanism performs the best, and Shrestha mechanism performs the second. Mathieu mechanism under-estimates the laminar flame speed, and all the other mechanisms overestimate the flame speed at different levels. Especially, the reaction mechanism developed by Klippenstein et al. and Konnov et al. have the maximum *RMSE* values larger than 10 and 19 cm/s, respectively.

Considering the above comparisons with experimental data under various conditions, the updated mechanism of Shrestha et al. [10] shows the best performances under different BRs, pre-heat temperatures, equivalence ratios, and pressures. This provides a reliable basis for the following quantitative measurement in the following flame calculations. Therefore, this mechanism is used in the following one-dimensional (1D), two-dimensional (2D) and three-dimensional (3D) calculations that are used to establish the flame database for HRRS identification.

2.2. 1D freely propagating premixed flames

Series of 1D freely propagating premixed flames (as shown in Fig. 5 (a)) are calculated using Cantera [46] under various equivalence ratios, BRs, initial pre-heat temperatures, and pressures. In particular, the

equivalence ratio varies from 0.6 to 1.6 with an interval of 0.05, covering the lean, stoichiometric, and rich conditions. The mole fraction of hydrogen in the fuel stream varies from 0 to 0.8 with an interval of 0.05. Three pre-heat temperatures, 300, 500, and 700 K, are considered to represent different pre-heat degrees. Three pressures, 1, 5, and 10 bar, are considered, covering the atmosphere, engine-like, and gas-turbine-like conditions. In total, there are $21 \times 21 \times 3 \times 3 = 3969$ 1D laminar flames calculated. The ‘MultiTransport’ transport model is used to account for the species diffusivities, and the Soret effect is neglected. The slope, curvature, and ratio for grid refinement are set as 3, 0.01, and 0.01, respectively, to confirm that there are more than 500 grid points across whole domain, which can provide enough resolutions for the reaction zones. The profiles of mole fractions of species, heat release rate, and reaction rates of each reaction are saved for the following kinetic analysis and establishing the flame database.

2.3. 2D turbulent premixed jet flames

To validate the identified HRRS in a *posterior* manner, several two-dimensional (2D) turbulent premixed flames of ammonia–hydrogen in a temporally evolving jet are calculated under various BRs, equivalence ratios, pressures, and pre-heat temperatures. The computational configuration is shown in Fig. 5(b), and the detailed operation conditions are listed in Table 1. Specifically, five BRs (0–0.8, interval:0.2), three equivalence ratios (0.8, 1.0, and 1.2 for lean, stoichiometric, and rich conditions), three pre-heat temperatures (300 K, 500 K and 700 K), three pressure (1 bar, 5 bar, and 10 bar), and three turbulent Reynolds numbers ($Re_t = 35.48, 53.22, \text{ and } 79.83$) are considered. Therefore, in total 13 cases are calculated. Note that from case 6 to case 13, the BR is set to be 0.4, which is justified from the previous research findings that at this blending ratio, the ammonia–hydrogen premixed flames have the similar combustion characteristics of methane [47,48]. The jet width (H) is set as 2 mm, and the computational domain has a length of 20H in each direction. The computational grid is uniform with a resolution of 20 μm in the low pressure cases and 10 μm in

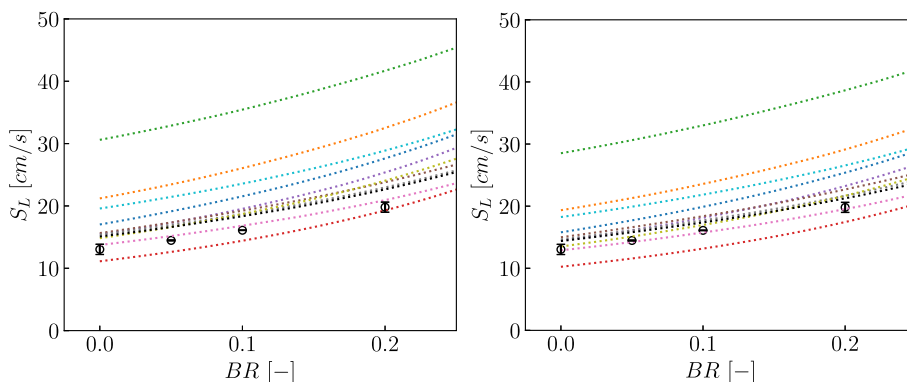


Fig. 4. Comparisons between the laminar flame speeds predicted with different reaction mechanisms (dash lines) and those measured in experiments (scatters) under different equivalence ratio and BRs ($T_{fresh} = 473$ K, $\phi = 1.1$). The line legend is same as that in Fig. 1, and the experimental data are collected from Shrestha et al. [10].

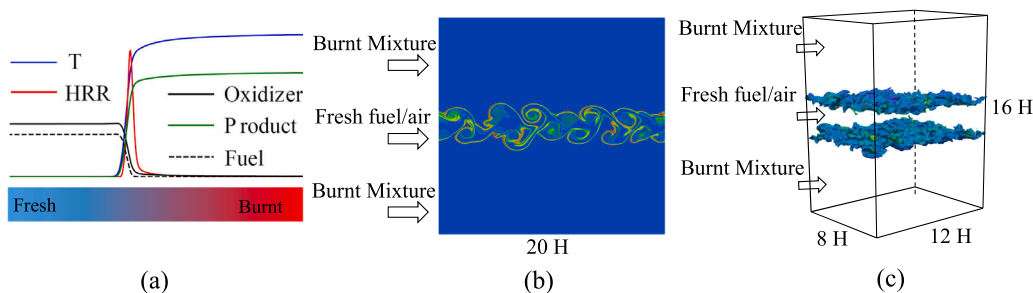


Fig. 5. Schematics of the computational configurations of (a) 1D freely propagating premixed flames, and premixed flames in 2D (b) and 3D (c) temporally evolving jet flows.

Table 1
Case settings for the 2D turbulent premixed flames in a temporally evolving jet.

Case	ϕ [-]	BR [-]	P [bar]	T_{fresh} [K]	Re_t [-]	Ka [-]
1	1.0	0.0	1.0	300	36.39	947.38
2	1.0	0.2	1.0	300	35.96	362.00
3	1.0	0.4	1.0	300	35.48	93.59
4	1.0	0.6	1.0	300	34.91	22.10
5	1.0	0.8	1.0	300	34.23	9.45
6	0.8	0.4	1.0	300	35.00	160.73
7	1.2	0.4	1.0	300	35.93	106.97
8	1.0	0.4	1.0	500	35.48	54.88
9	1.0	0.4	1.0	700	35.48	40.76
10	1.0	0.4	5.0	500	24.07	24.24
11	1.0	0.4	10.0	500	18.91	8.67
12	1.0	0.4	1.0	300	53.22	171.94
13	1.0	0.4	1.0	300	79.83	315.87

the high pressure and turbulent Reynolds number cases, which could provide more than 10 grid points across the flame thickness and well resolve the Kolmogorov scale. The central jet is composed of fresh premixed fuel/air mixture, and the co-flow features a burnt mixture of the fresh premixed mixture, which is the similar as that in our previous studies [49,50]. The absolute jet velocity (U) is 80 m/s, and an isotropic turbulence of an intensity of 4% of the absolute jet velocity and an integral scale of $H/6$ are superimposed on the mean velocity profile to accelerate the development of the shear layer. The Courant number is set to be less than 0.5, and the total calculation physical time is five flow periods. Here one flow period time is defined as $t_j = L_x/U_j$. L_x is the length of the domain in the stream-wise direction. U_j is the absolute jet velocity calculated using $U_{central} - U_{pilot}$, where $U_{central}$ and U_{pilot} are the velocities of the central fuel/air and pilot streams, respectively.

All calculations are conducted on the supercomputer FUGAKU with an in-house solver developed based on OpenFOAM [51], which has been validated with the experimental measurements and detailed chemistry solutions in our previous studies [52–54], and the species diffusivity is considered with the mixture-averaged method developed

by Ref. [55]. In the future work, the authors will further validate the codes and solvers with experimentally investigated target ammonia flames. The spatial integration terms are discretized with a second-order central differencing scheme, and the time integration terms are discretized with a second-order implicit scheme. For each low pressure and low Reynolds number case, the complete computation time is about 40 h, by parallel computation using 480 cores (12 nodes). For each high pressure (5 and 10 bar) and high Reynolds number case, the whole computation time is about 360 h by parallel computation using 1920 cores (48 nodes).

2.4. 3D turbulent premixed jet flame

As many previous studies indicated that 2D configuration neglects the vortex stretch in the third direction with the loss of small-scale fluctuations, which might results in a shorter auto-ignition time, more uniform reactions, and a higher heat release rates [56,57]. The present study also calculated a premixed flame of ammonia–hydrogen in a 3D temporally evolving jet under the atmosphere condition, as shown in Fig. 5(c). Note that since the computational cost of the 3D-DNS is extremely expensive, it is computationally unfordable to calculate several 3D cases similar as those in the 2D flames. The fuel stream in the center jet is composed of 40% H_2 and 60% NH_3 , with a temperature of 300 K and an equivalence ratio of 1.0. The main configurations are similar as those of the 2D flames. The difference is that the jet width (H) is 0.85 mm, and the computational domain has a size of $12H \times 16H \times 8H$. The turbulent Reynolds and Karlovitz numbers are 15.08 and 143.56, respectively. A uniform grid resolution of $17 \mu m$ ($600 \times 800 \times 400$) is used for meshing the computational domain, and the total grid number is 192 million. The Courant number is also set to be less than 0.5, and the total calculation physical time is five flow periods. The calculation of the 3D premixed flame used the same solver introduced above, by parallel computation on the supercomputer FUGAKU using 8000 cores (400 nodes), and the actual computational time is about 400 h.

Table 2
Detailed procedures to identify the optimal HRRS.

Inputs: Series of 1D premixed flame profiles
Outputs: Mean $Z(v)$ values for all the flames
Parameter spaces [range(interval)]:
BR : 0-0.8 (0.1); P : 1, 10 bar; ϕ : 0.6-1.6 (0.1); T_{fresh} : 300, 700 K; p , q : 0-3 (0.1,0.01)
Loop p:
Loop q:
Loop BR:
Loop P:
Loop ϕ:
Loop T_{fresh}:
1. Normalize HRR, and species mole fractions([A] and [B]);
2. Reconstruct HRR using $[A]^p[B]^q$;
3. Calculate $Z(v p, q, BR, P, \phi, T_{fresh})$ value for each flame profile;
4. Obtain mean $f(v p, q)$ value for all the conditions;
5. Identify the minimum $f(v p, q)$ value and its corresponding p and q values.

3. Approaches for identifying heat release rate surrogates

3.1. Error quantification method

In the present study, the discrepancy between heat release rates calculated in the DNS and reconstructed with the HRRSs is measured with the indicators proposed by Nikolaou and Swaminathan [20] and further modified by Chi et al. [29]. For the 1D flames, it can be expressed as,

$$Z(v) = \frac{1}{L_x} \int_x \left(\frac{\dot{Q}(x)}{\max(\dot{Q}(x))} - \frac{v(x)}{\max(v(x))} \right)^2 dx \quad (1)$$

where $Z(v)$ is the reconstruction error, dx is the cell length, v is the selected variable (HRRS), and L_x is the width of 1D computational domain. $\dot{Q}(x)$ and $v(x)$ are the heat release rate and variable value at location x , respectively. $\max(\dot{Q}(x))$ and $\max(v(x))$ represent the maximum heat release rate and variable value across the whole domain, respectively. For the 2D and 3D temporal evolving flames, its formula is expressed as in a temporal form [29],

$$Z(v, t) = \frac{1}{V} \int_V \left(\frac{\dot{Q}(x, y, z, t)}{\max(\dot{Q}(x, y, z, t))} - \frac{v(x, y, z, t)}{\max(v(x, y, z, t))} \right)^2 dV \quad (2)$$

where $Z(v, t)$ is the reconstruction error at time t using variable v , dV is the cell volume, and V is total volumes of all samples. $\dot{Q}(x, y, z, t)$ and $v(x, y, z, t)$ are the heat release rate and variable value at location (x, y, z) and time t , respectively. $\max(\dot{Q}(x, y, z, t))$ and $\max(v(x, y, z, t))$ represent the maximum heat release rate and variable value across the whole domain at time t , respectively. Since the co-flow stream is composed of a burnt mixture, the heat release rate is very small, which might significantly affect the error measurement results. Therefore, only regions with HRR value larger than 1% of the maximum value are considered in the error quantification (for both the 1D, 2D, and 3D flames).

3.2. HRRS identification method

In the viewpoint of experimental measurement, those species are easier to be measured could be potential candidates for reconstructing heat release rate. Considering the fact that simultaneous measurements of multiple species in the experiments are very hard, the present study only considers the combination of two candidate species, for example A and B. The combination of two species with non-unity exponents are expressed as $[A]^p[B]^q$, and its performance on reconstructing HRR under various conditions can be accessed by calculating the mean $Z(v|p, q)$ values under all the parameter spaces (blending ratio, pressures, equivalence ratio, and initial temperatures). The optimal HRRS has the minimum $Z(v|p, q)$ value. The detailed procedures to identify the optimal HRRS are introduced in Table 2.

Firstly, the profiles of heat release rate and species mole fractions are normalized with their maximum values, which is consistent with

the definition in Eq. (1). Then, the HRR profiles are reconstructed with the designed HRRS, $[A]^p[B]^q$, and $Z(v|p, q, BR, P, \phi, T_{fresh})$ is calculated for each flame profile using Eq. (1). After looping all the parameter spaces (BR, pressure, equivalence ratio, and initial temperature), the mean error $f(v|p, q)$ can be obtained using Eq. (3).

$$f(v|p, q) = \frac{1}{N_{BR} N_P N_\phi N_{T_{fresh}}} \sum_1^{N_{BR}} \sum_1^{N_P} \sum_1^{N_\phi} \sum_1^{N_{T_{fresh}}} \frac{Z(v|p, q, BR, P, \phi, T_{fresh})}{Z(v|1, 1, BR, P, \phi, T_{fresh})} \quad (3)$$

where N_{BR} , N_P , N_ϕ , and $N_{T_{fresh}}$ are the numbers of blending ratio, pressure, equivalence ratio, and initial temperatures considered. Note that to make a direct comparison with HRRS using the unity exponents, the error value is normalized with the error at unity exponents, which is same as that in the study of Song et al. [27]. Finally, the identification of optimal HRRS is to find the minimum $f(v|p, q)$ among different combinations of p and q values in a certain range. Only parts of the 1D flames (see parameter spaces in Table 2) are selected for identification of the optimal HRRS, and the rest samples will be used for a *posterior* analysis. Note that 1D freely propagating flame with non-unity Lewis numbers (detailed diffusion considered) was proven to be able to reproduce the preferential diffusion effect in our previous flamelet LES study of a low-swirl burner [58], and the detailed diffusion has already been considered in the present calculations of 1D flames. It might be better to use 2D turbulent flame data as the database to consider both the flame curvature and preferential diffusion effects, as the study of Chi et al. [29]. However, to identify suitable HRRS for premixed ammonia-hydrogen flames under various conditions, the parameter spaces should cover various equivalence ratios, pressures, pre-heated temperatures, and blending ratios. To construct a comprehensive database, the computational cost would be huge even using 2D calculations with detailed chemistry. Therefore, the authors turned to establish the database using several thousands of 1D flames. For the p and q values, the grid-search optimization method is used in the range of 0 to 3. Specifically, a relative coarse interval (0.1) is firstly used to roughly obtain the approximate range of optimal solution, and then a fine interval (0.01) is used to scan the approximate range to find the optimal solution with a much higher resolution. This two-step grid-search method is employed here because there are various operation conditions considered, and the optimization process would be very time-consuming with a fine resolution in the full space. The identified optimal HRRS is further validated in a *posterior* manner on the rest 1D, 2D, and 3D flames.

4. Results and discussion

4.1. Heat release rate characteristic

In this part, the effects of BR, equivalence ratio, pre-heat temperature, and pressure on HRR characteristics are analyzed and explored from series of the 1D premixed flames.

4.1.1. Effect of blending ratio

Fig. 6 shows the correlation between profiles of reaction rates and heat release rate under different BRs. Note that for the error plots, only the minimum 15 reactions are shown for brevity (this is same for the following figures). The highly-correlated reactions vary as the blending ratio increases, as shown in Fig. 6(a). Specifically, NH_2 -involved reactions are highly correlated with heat release rate for pure ammonia flame, such as $\text{NH}_2 + \text{O} \rightleftharpoons \text{NH} + \text{OH}$ (duplicate reactions with different kinetic parameters) and $\text{NH}_2 + \text{OH} \rightleftharpoons \text{H}_2\text{O} + \text{NH}$. With the increasing of BR, the H-involved reactions are found to be more correlated with HRR profiles, such as $\text{H}_2 + \text{O} \rightleftharpoons \text{H} + \text{OH}$ and $\text{H} + \text{HO}_2 \rightleftharpoons 2\text{OH}$. Fig. 6(b) shows the reconstruction performance using profiles of reaction rates. Note that only the best five reactions are plotted for a clear observation. It is

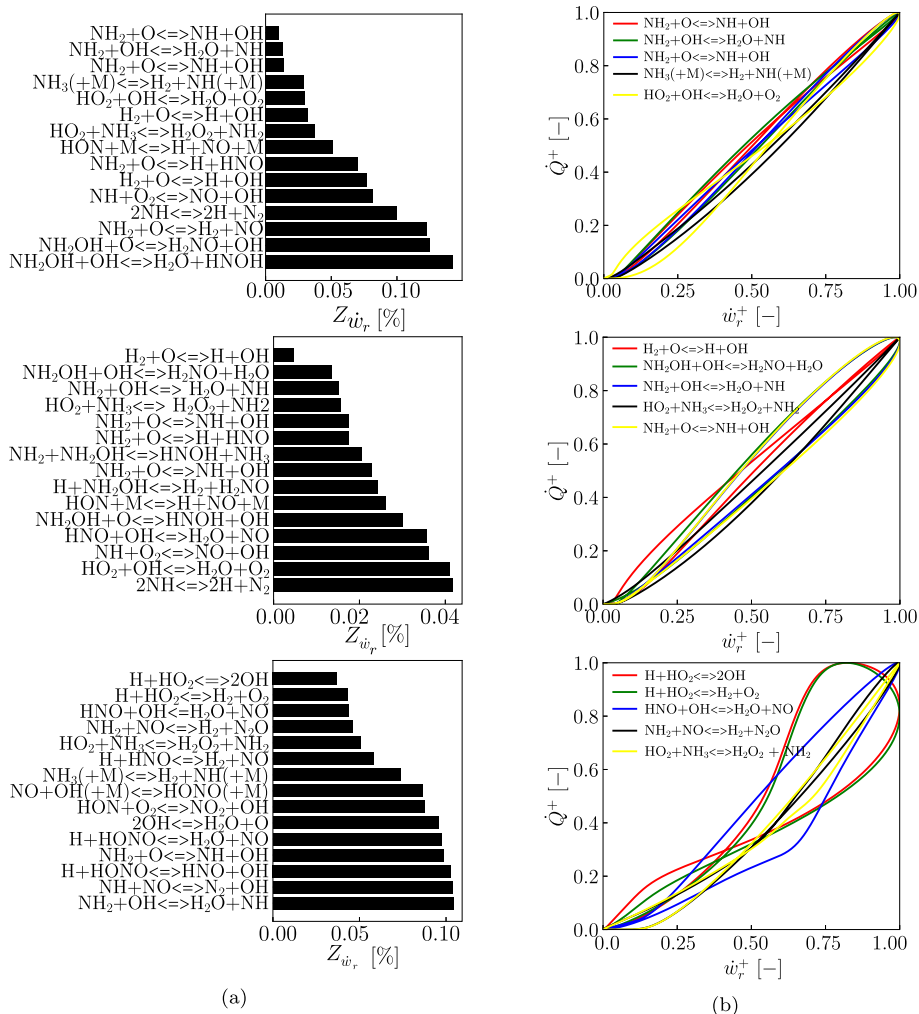


Fig. 6. Correlations between the reaction rates of elementary reactions and heat release rate profiles under different BRs: (a) $Z_{\dot{w}_r}$ and (b) plots of \dot{Q}^+ and \dot{w}_r^+ . Top to bottom: BR = 0, 0.4, and 0.8.

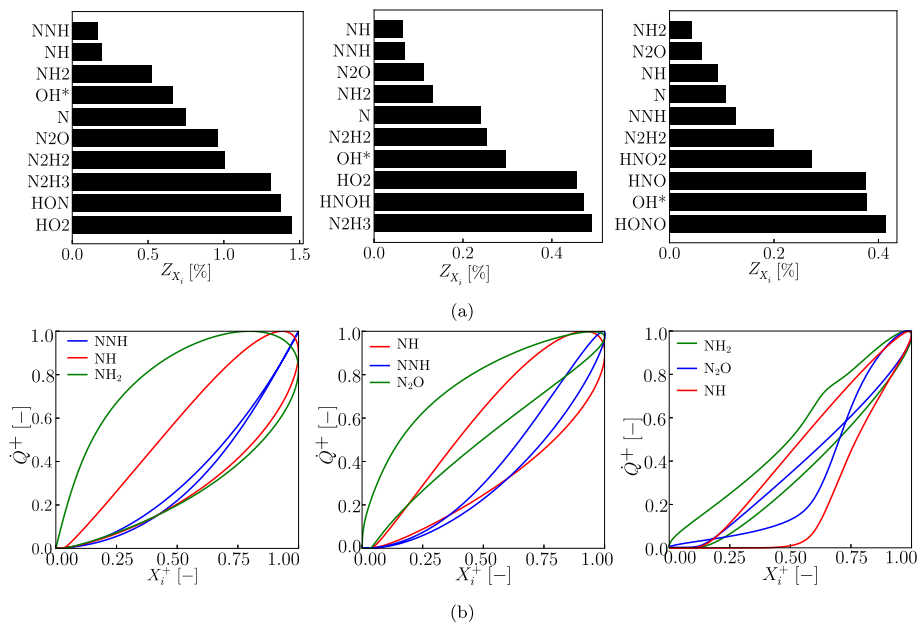


Fig. 7. Correlations between the reaction rates of elementary reactions and heat release rate profiles under different BRs: (a) Z_{X_i} and (b) plots of \dot{Q}^+ and X_i^+ . Left to right: BR = 0, 0.4, and 0.8.

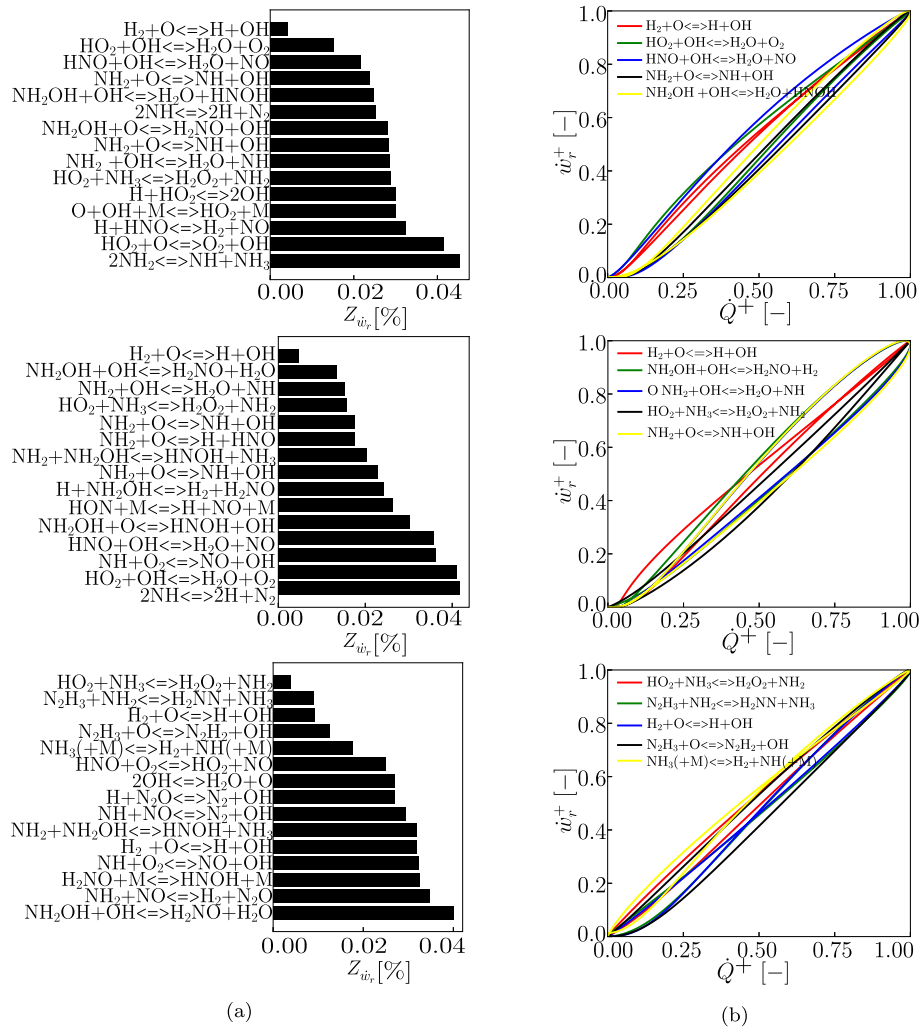


Fig. 8. Correlations between the reaction rates of elementary reactions and heat release rate profiles under different equivalence ratios: (a) Z_{w_i} and (b) plots of \dot{Q}^+ and w_r^+ . Top to bottom: $\phi = 0.6, 1.0, \text{ and } 1.6$.

found that at relatively low BRs ($BR = 0$ and 0.4), the HRR profiles can be well reproduced with errors less than 0.02% measured with Eq. (1) in Section 3.1. As for high blending ratio case, the reconstruction errors becomes much larger, which indicates the correlation between reaction rates and HRR is much weaker in the ammonia–hydrogen flames with high BRs.

Fig. 7 shows the reconstruction performances with single species. Note that only the best ten species are considered here for brevity. It is found that as blending ratio increases, the reconstruction performance of each species also changes; NH and NH_2 can make well reconstructions under various BRs with small errors. This is different from HRR reconstructions using the reaction rate in Fig. 6(a) and indicates that NH and NH_2 might be potential species that could be used to reconstruct HRR under various BRs.

4.1.2. Effect of equivalence ratio

Fig. 8 shows the correlations between profiles of reaction rates and HRR under various equivalence ratios (lean-to-rich: $0.6, 1.0, \text{ and } 1.6$). It is found that equivalence ratio has obvious effects on the HRR reconstruction when using reaction rate profiles. In particular, under lean and stoichiometric conditions, reaction rate profiles of OH, NH, and NH_2 involved reactions, such as $H_2+O \rightleftharpoons H+OH$ and $NH_2+O \rightleftharpoons NH+OH$, correlate well with the HRR profiles. While for the rich condition, NH_3 and NH_2 involved reactions are superior for HRR reconstruction. This

might be caused by the insufficient oxygen required for full oxidation of the fuel, resulting in rich intermediate species, such as NH_2 and OH.

As for the reconstruction using single species, similar trends as those using reaction rate profiles can also be found as shown in Fig. 9. Under lean and stoichiometric conditions, species profiles of NH, NNH, and NH_2 can reconstruct the HRR profiles with small errors. While for rich conditions, this superiority does not keep, and O, N_2H_2 , and H_2NN profiles have better performances for HRR reconstruction. However, those species are generally hard to be measured in the experiments, which might bring huge challenges to reconstruct HRR for premixed ammonia–hydrogen flames under rich conditions.

4.1.3. Effect of pre-heat temperature

Fig. 10 shows the reconstruction performances using reaction rates under different pre-heat temperatures. It is found that the reaction routines, whose reaction rates correlate well with HRR, are nearly same under different pre-heat temperatures, with slight changes on the ranking order. This indicates that pre-heat temperature does not have significant effects on the overall reaction pathways and HRR reconstructions. Specifically, profiles of some OH-involved reactions, such as $H_2+O \rightleftharpoons H+OH$ and $NH_2+OH \rightleftharpoons H_2O+NH$, correlates well with the HRR profiles for various pre-heat temperatures. As for the reconstruction using single species, this conclusion is still valid as shown in Fig. 11. Species profiles of NH_2 , NH, and N_2O correlates well with HRR profiles under various pre-heat temperatures.

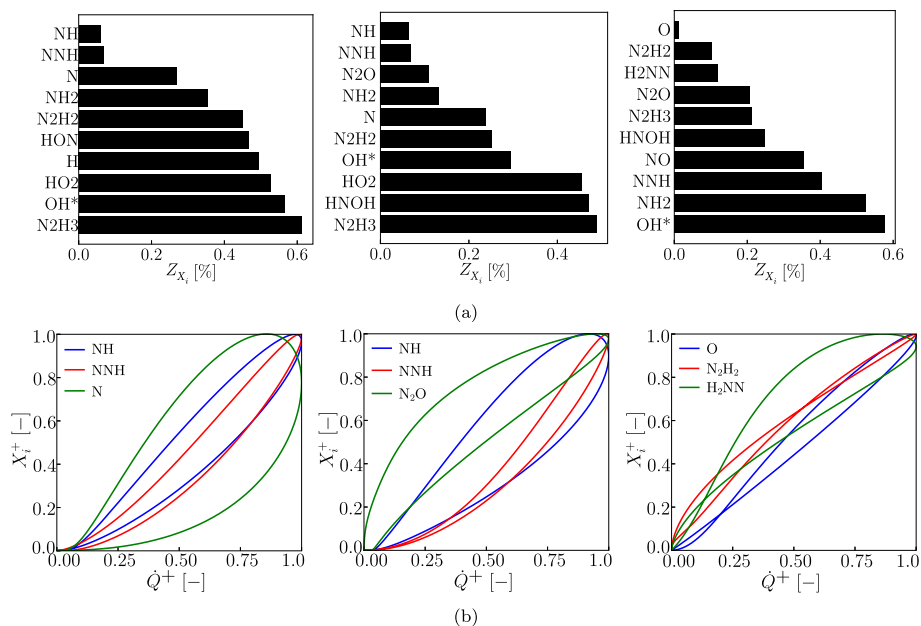


Fig. 9. Correlations between the reaction rates of elementary reactions and heat release rate profiles under different equivalence ratios: (a) Z_{X_i} and (b) plots of \dot{Q}^+ and X_i^+ . Left to right: $\phi = 0.6, 1.0,$ and 1.6 .

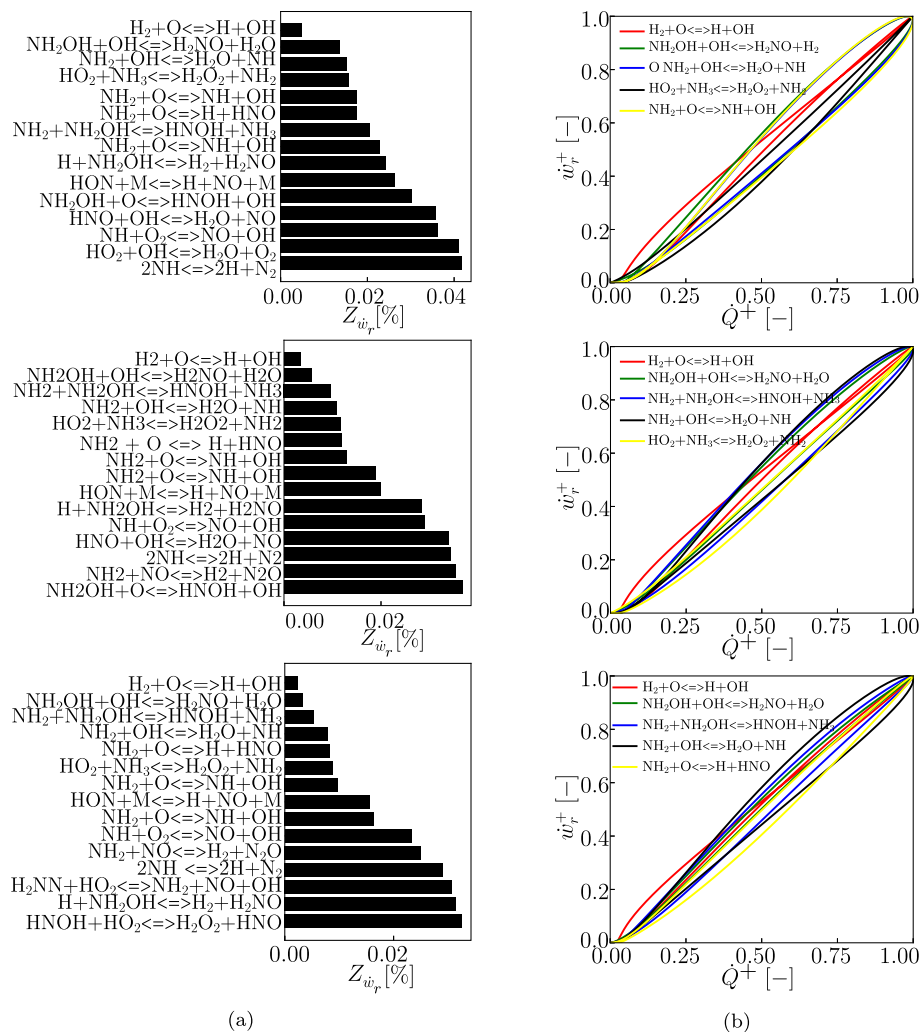


Fig. 10. Correlations between the reaction rates of elementary reactions and heat release rate profiles under different pre-heat temperatures: (a) $Z_{w_{ir}}$ and (b) plots of \dot{Q}^+ and w_{ir}^+ . Top to bottom: $T_{fresh} = 300, 500,$ and 700 K.

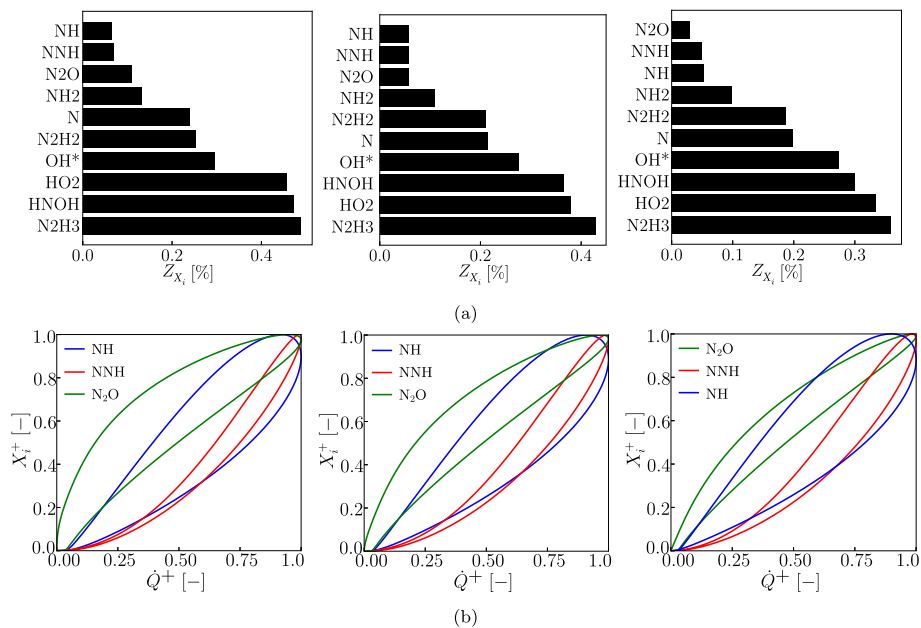


Fig. 11. Correlations between the reaction rates of elementary reactions and heat release rate profiles under different pre-heat temperatures: (a) Z_{X_i} and (b) plots of \dot{Q}^+ and X_i^+ . Left to right: $T_{jresh} = 300, 500, \text{ and } 700 \text{ K}$.

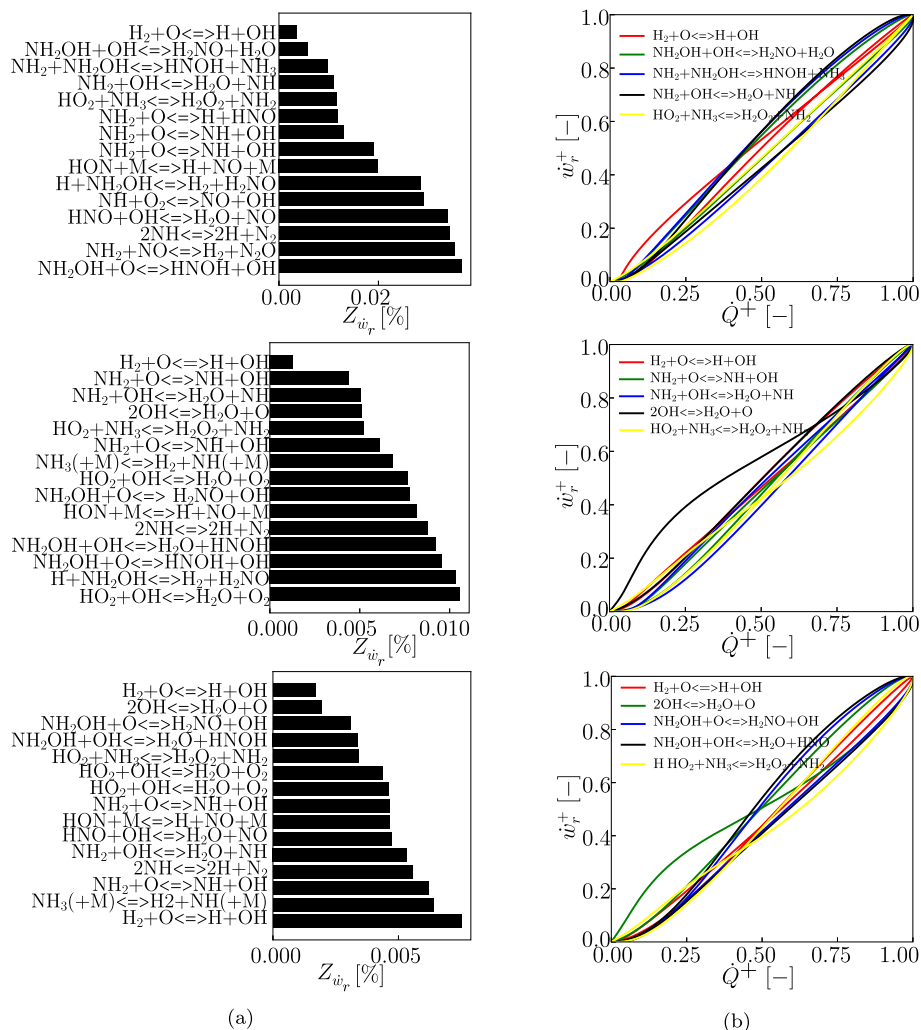


Fig. 12. Correlations between the reaction rates of elementary reactions and heat release rate profiles under different pressures: (a) Z_{w_r} and (b) plots of \dot{Q}^+ and w_r^+ . Left to right: $P = 1, 5, \text{ and } 10 \text{ bar}$.

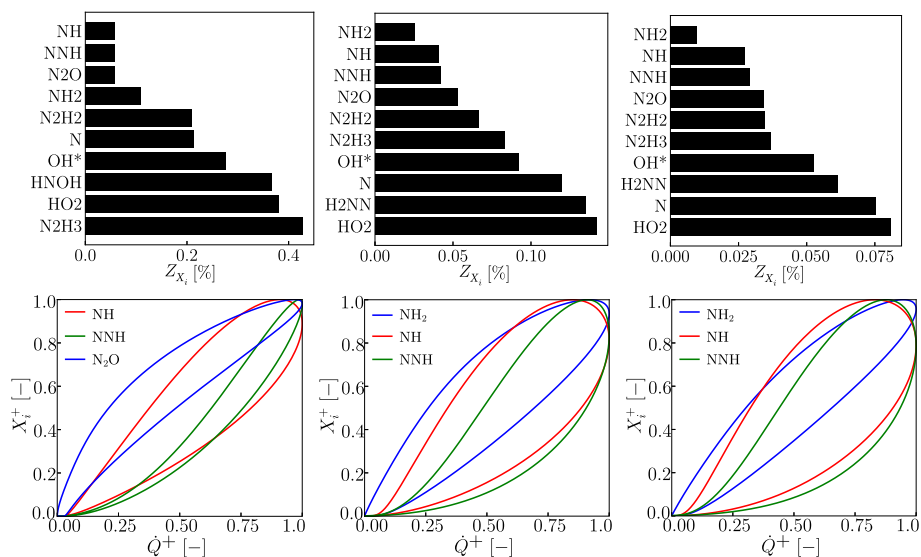


Fig. 13. Correlations between the reaction rates of elementary reactions and heat release rate profiles under different pressures: (a) Z_{X_i} and (b) plots of \dot{Q}^+ and X_i^+ . Left to right: $P = 1, 5,$ and 10 bar.

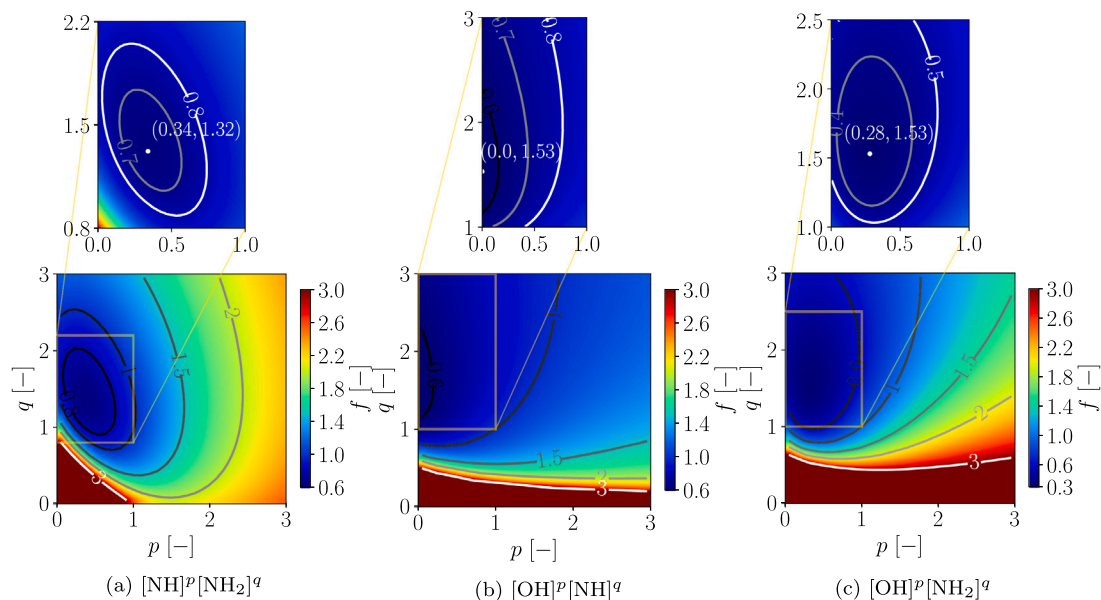


Fig. 14. Normalized mean error for HRR reconstruction using different species combinations with different p and q values.

4.1.4. Effect of pressure

Fig. 12 shows the correlation between profiles of reaction rate and HRR under different pressures (1, 5, and 10 bar). The most correlated reaction does not change but the ranking order slightly changes with the increasing of pressure. Overall, reaction profiles of OH-involved reactions, such as $H_2 + O \rightleftharpoons H + OH$ and $NH_2 + O \rightleftharpoons NH + OH$, correlate with the HRR profiles well.

As for the reconstruction performances using single species, pressure also does not have significant effects as shown in Fig. 13. Specifically, species profiles of NH, NNH, N_2O , and NH_2 have a better performance in reconstructing HRR profiles than other species, and the reconstruction errors are slightly decreased as pressure increases.

4.2. HRRs for ammonia-hydrogen premixed flames

The species candidates that can be used to develop HRRS should have the following characteristics: (1) the species candidates should

have a relatively high correlation with HRR; (2) the species candidates should be measurable through either fluorescence or chemiluminescence approaches [17,18]. Considering the analysis from the one-dimensional profiles under various conditions, the three species, NH, NH_2 , and OH, are selected as the species candidates to reconstruct HRR as they both have close correlations with the HRR fields and have proven to be measured through both fluorescence and chemiluminescence approaches in the previous experimental studies of ammonia flames [17,18,59,60]. Three species combinations ($[NH]^p[NH_2]^q$, $[NH]^p[OH]^q$ and $[NH_2]^p[OH]^q$) are considered. Fig. 14 shows the normalized mean errors of HRRSs using different species combinations and exponent values. The lower bottom plots show the rough scan results with an interval of 0.1, and the upper enlarged plots show the fine scan results within narrow ranges that are determined based on the rough scan. For the species combination of $[NH]^p[NH_2]^q$, when q value is fixed, the mean error first decreases and then increase with p value increases. The regions of small errors locates in the range of

Table 3
Minimum mean errors for the three species combinations.

Species combinations	$[\text{NH}]^p[\text{NH}_2]^q$	$[\text{NH}]^p[\text{OH}]^q$	$[\text{NH}_2]^p[\text{OH}]^q$
$Z_{\text{mean}}^{\text{min}} [-]$	7.50×10^{-4}	2.41×10^{-3}	6.90×10^{-4}

$p \in [0,1]$ and $q \in [0.8,2.2]$, as shown in Fig. 14(a). The corresponding minimum values of the mean errors are listed in Table 3. After a fine scan, the optimal p and q values are 0.32 and 1.32, respectively, and the minimum mean error is about 7.50×10^{-4} . For the species combination of $[\text{NH}]^p[\text{OH}]^q$, the mean error decrease with the increasing of q when p value is larger than 0.6. There is an obvious region of low errors in the range of $p \in [0,1]$ and $q \in [1,3]$, as shown in Fig. 14(b). The fine scan results show that the optimal exponents are 0.0 and 1.53 for p and q , respectively, and the mean error is about 2.41×10^{-3} . For the species combination of $[\text{NH}_2]^p[\text{OH}]^q$, the mean error has the similar trends as those of $[\text{NH}]^p[\text{OH}]^q$. The low error region locates in the range of $p \in [0,1]$ and $q \in [1,2.5]$ from the rough scan results, as shown in Fig. 14(c). The optimal p and q values are 0.28 and 1.53, respectively, and the minimum mean error is about 6.90×10^{-4} . Considering that the minimum mean error of species combination of $[\text{NH}_2]^{1.53}[\text{OH}]^{0.28}$ is the lowest among all the three combinations, this species combination is selected as the optimal HRRS, which could give accurate HRR reconstructions for all the conditions and will be validated in a posterior manner in the following.

4.3. A posterior analyses

In this section, the identified optimal HRRS will be validated on the remaining 1D (those are not used in the identification process) and 2D/3D premixed flames in a temporally evolving planer jet. Each part will be introduced in turn. The predictions of the two HRRSs recommended in the study of Cheng et al. [29], are also plotted for comparisons.

4.3.1. 1D freely propagation premixed flames

Fig. 15 shows the comparisons of the reconstruction of heat release rate using the optimal HRRs developed in the present study and two HRRSs recommended by Chi et al. [29] (named Chi-1 and Chi-2) under various conditions. Note that only some conditions are plotted here for brevity. The error values of those conditions are listed in Table 4. Figs. 15(a1–c1) show the performances under different initial temperature ($P = 5$ bar, $\phi = 1.0$, $BR=0.6$). As the initial temperature increases, reconstruction performance of the three HRRSs are both good and stable, and the error values are both below 4×10^{-4} . The present developed HRRS performs slightly better, with the minimum error values. When the pressure increases from atmospheric to elevated pressures, the developed HRRS keeps the superiority against two previous HRRS, especially at 10 bar, the error magnitude is one order smaller, as shown in Fig. 15(a2–c2). As for lean, stoichiometric, and rich conditions, the present HRRS performs slight better at lean and stoichiometric conditions. But under the rich condition, its performance is comparable to the Chi-1 HRRS and better than Chi-2 HRRS, as shown in Fig. 15(a3–c3). As for different BRs, the present HRRS is generally worse than the previous two HRRSs, and the error difference gradually decreases, as shown in Figs. 15(a4–c4). This might be attributed to that the present HRRS is developed by finding the minimum mean error through looping all the conditions; as seen from Fig. 7, flames with high BRs are much harder to be represented with the selected species. Table 4 also listed the mean and standard errors of the three HRRSs on the whole a posteriori 1D flame database. The present developed HRRS has a mean error of 5.50×10^{-4} , which is about two and five times smaller compared with those of Chi-1 and Chi-2 HRRSs, respectively. Moreover, the standard deviation is about three and seven times smaller than those of the other two HRRSs. This indicates that the present developed HRRS can give accurate HRR reconstruction and its performance is much more stable under various conditions.

Table 4
Error statistics of the HRR reconstruction under various conditions.

Conditions		$P = 5$ bar, $\phi = 1$, $BR = 0.6$		
		$T_{\text{fresh}} = 300$ K	$T_{\text{fresh}} = 500$ K	$T_{\text{fresh}} = 700$ K
$Z(v) [-]$	Present	1.48×10^{-4}	2.34×10^{-4}	1.50×10^{-4}
	Chi-1	2.27×10^{-4}	3.73×10^{-4}	2.35×10^{-4}
	Chi-2	1.78×10^{-4}	3.10×10^{-4}	1.95×10^{-4}
Conditions		$T_{\text{fresh}} = 500$ K, $\phi = 1.45$, $BR = 0.6$		
		$P = 1$ bar	$P = 5$ bar	$P = 10$ bar
$Z(v) [-]$	Present	1.98×10^{-4}	1.60×10^{-3}	4.30×10^{-5}
	Chi-1	2.85×10^{-4}	2.87×10^{-3}	6.61×10^{-4}
	Chi-2	3.18×10^{-4}	2.05×10^{-3}	7.90×10^{-4}
Conditions		$T_{\text{fresh}} = 500$ K, $P = 10$ bar, $BR = 0.5$		
		$\phi = 0.8$	$\phi = 1.0$	$\phi = 1.2$
$Z(v) [-]$	Present	1.22×10^{-4}	1.39×10^{-4}	1.39×10^{-4}
	Chi-1	1.48×10^{-4}	3.66×10^{-4}	1.31×10^{-4}
	Chi-2	7.00×10^{-4}	1.19×10^{-3}	1.85×10^{-4}
Conditions		$T_{\text{fresh}} = 500$ K, $P = 5$ bar, $\phi = 1.0$		
		$BR = 0.0$	$\phi = 0.2$	$\phi = 0.4$
$Z(v) [-]$	Present	2.59×10^{-4}	5.09×10^{-4}	3.00×10^{-4}
	Chi-1	2.02×10^{-4}	4.75×10^{-4}	2.90×10^{-4}
	Chi-2	1.48×10^{-4}	3.33×10^{-4}	1.88×10^{-4}
Conditions		The whole database (a posterior)		
HRRS	Present	Chi-1	Chi-2	
$Z(v)_{\text{mean}} [-]$	5.50×10^{-4}	1.16×10^{-3}	2.71×10^{-3}	
$Z(v)_{\text{std}} [-]$	1.14×10^{-4}	3.26×10^{-4}	7.61×10^{-4}	

4.3.2. 2D temporally evolving planer jet flames

The developed HRRS is further validated on several 2D flames listed in Table 1. For brevity, only case 3 results are plotted. Fig. 16 shows comparisons of the HRR predicted in the DNS and reconstructed using the present developed HRRS at three time instants ($\tau^* = 1, 2$, and 3) of case 3. τ^* is defined as t/t_j , where t_j is one flow period, defined in Section 2. The predictions of the two HRRSs recommended by Chi et al. [29] are also plotted here for comparisons. At $\tau^* = 1$, the mixing layer is still in the developing phase, thus the high HRR regions are narrow and smooth. The present developed HRRS can better reconstruct the HRR field than the two previous HRRSs. Specifically, the absolute error of the present developed HRRS is within 0.2, while those of the two previous HRRSs are much larger, especially Chi-1. With the further development of the mixing layer ($\tau^* = 2$ and 3), the HRR distribution is more wrinkled, and there is an obvious non-uniform spatial distribution. Specifically, The regions of high HRR are concentrated in the area with relatively high curvature of flame stretch, whether the curvature is positive or negative, as shown in Fig. 17. This might relate to the preferential diffusion effect due to the existence of hydrogen in the fuel side, which has been pointed out in previous studies [29,30]. A quantitative statistic on the flame curvature is made as shown in Fig. 18. The flame curvature κ is calculated based on the flame surfaces identified from the progress variables calculated by $c = (T - T_{\text{fresh}})/(T_{\text{burnt}} - T_{\text{fresh}})$, where T_{fresh} and T_{burnt} are the fresh and burnt temperatures. Specifically, three progress variable values (0.3, 0.5, and 0.7) are considered. The present developed HRRS performs quite stable under different curvatures, and its accuracy is better than the other two previous HRRSs. It is also interesting that the present developed HRRS has opposite regions of negative and positive errors compared with those of Chi-1 HRRS, which can be attributed to different distributions of HRR in the spaces of species candidates and power coefficient values of $[\text{NH}]$ and $[\text{NH}_2]$ in the HRRS formulas. Overall, the present HRRS also performs better than the two previous HRRSs, with smaller absolute errors. Especially, the non-uniform distribution caused by preferential diffusion can be well represented by the present

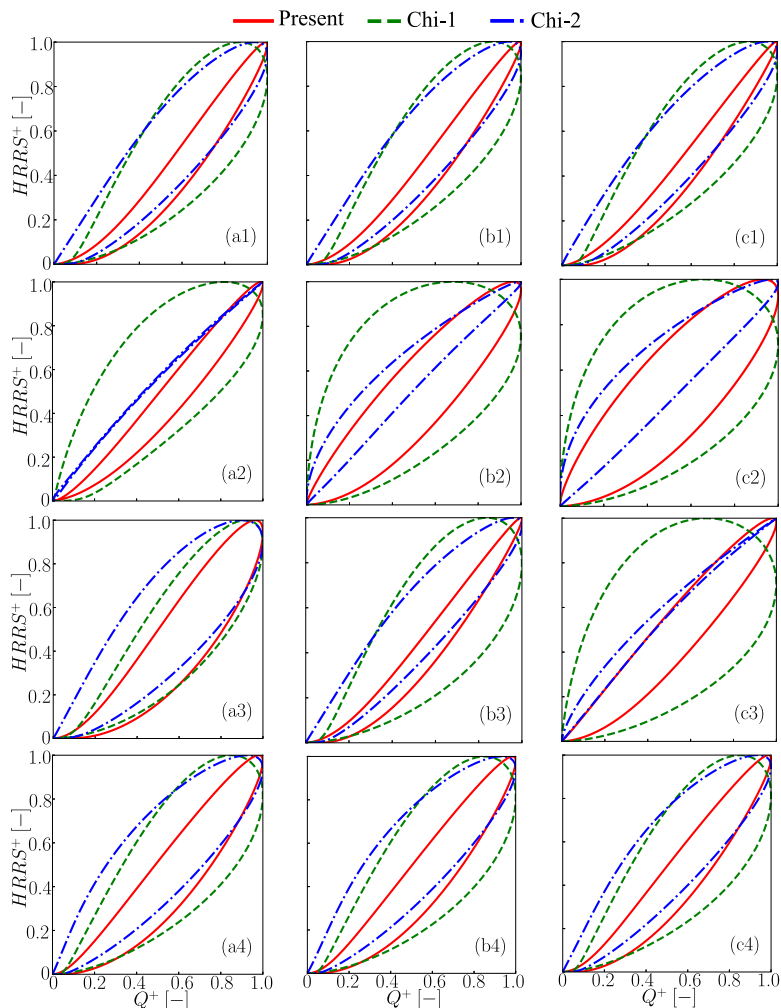


Fig. 15. Comparisons of the HRRS predictions with HRR profiles under various conditions: (a1–c1) $T_{fresh} = 300, 500, \text{ and } 700$ K at $P = 5$ bar, $\phi = 1$, and $BR = 0.6$; (a2–c2) $P = 1, 5, \text{ and } 10$ bar at $T_{fresh} = 500$ K, $\phi = 1.45$, and $BR = 0.6$; (a3–c3) $\phi = 0.8, 1.0, \text{ and } 1.2$ at $T_{fresh} = 500$ K, $P = 10$ bar, and $BR = 0.5$; (a4–c4) $BR = 0, 0.2, \text{ and } 0.4$ at $T_{fresh} = 500$ K, $P = 5$ bar, and $\phi = 1.0$.

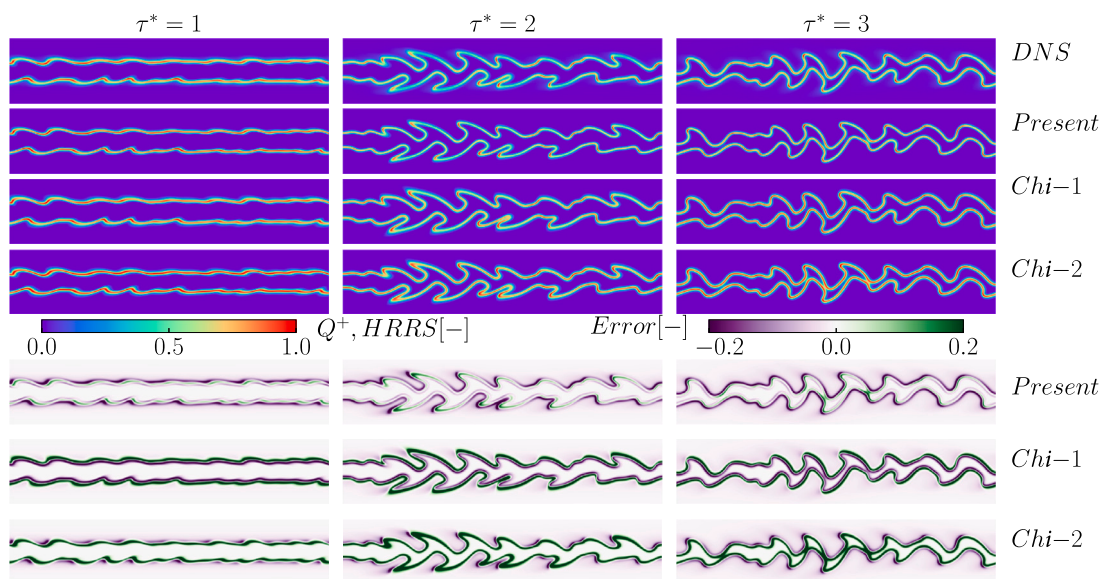


Fig. 16. Comparisons of the heat release rate predicted in the DNS and reconstructed using the present developed HRRS at three time instants (case 3). The predictions of the two HRRSs recommended by Chi et al. [29] are also plotted here for comparisons. The last three rows show the absolute errors of the reconstructions.

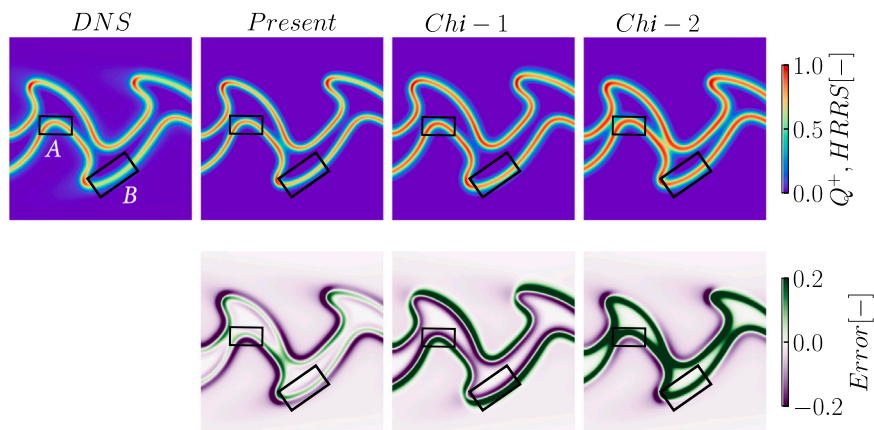


Fig. 17. Enlarged HRR fields obtained from the DNS and reconstructed using the present developed HRRS and two previous HRRSs recommended by Chi et al. [29]. The lower row plots the absolute error between the actual and reconstructed HRR.

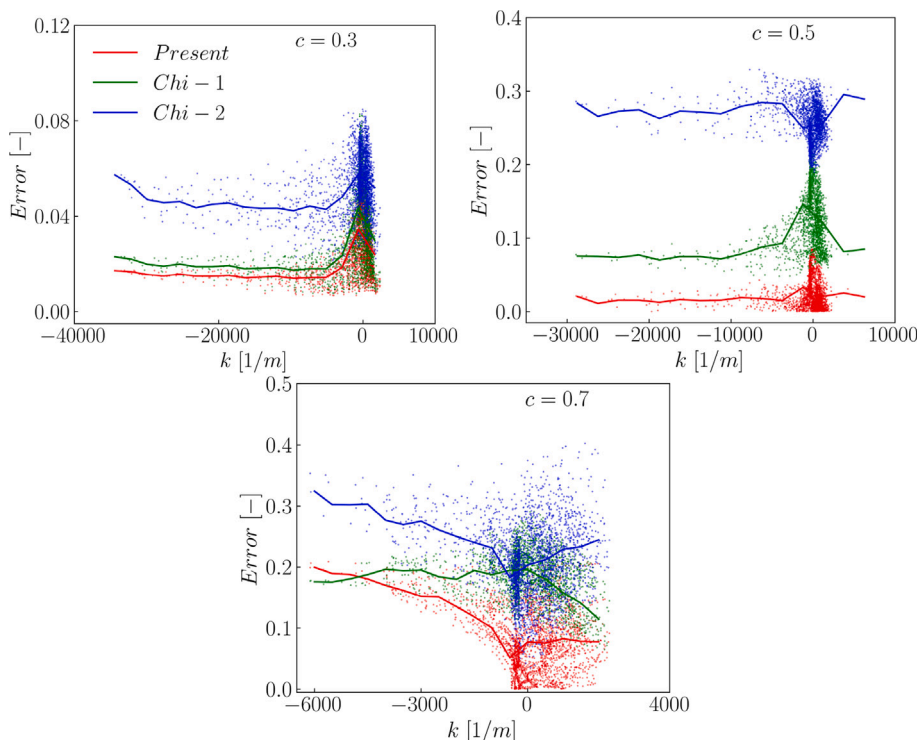


Fig. 18. Prediction errors under different curvatures calculated based on the flame surface identified using the three progress variable values (c , 0.3, 0.5 and 0.7).

developed HRRS, as shown in boxes A and B in Fig. 17. But Chi-1 HRRS can only partially reproduce this effect, and Chi-2 HRRS gives a much uniform high HRR reconstruction, which means that the preferential diffusion effect cannot be well reproduced.

Fig. 19 shows comparisons of temporal evolution of the reconstruction errors using the developed HRRS and two previous HRRSs. For different equivalence ratios, the present developed HRRS performs well at all the lean, stoichiometric, and rich conditions. Its prediction errors are all less than 0.001 and temporally stable, as shown in Fig. 19(a). The errors of Chi-1 and Chi-2 HRRSs are obviously larger and increased or decreased temporally. As for various initial temperatures, the superiority of the developed HRRS still remains, and the error values and trends are similar as seen in Fig. 19(b). Fig. 19(c) shows the performances of the HRRSs under different BRs. Note that under high

BR cases ($BR = 0.6$ and 0.8), the flame gets ignited very fast, so there are few temporal points for statistics. It is found that the present developed HRRS also performs well temporally under various BRs. However, the reconstruction errors of the Chi-1 HRRSs are large in the earlier stage, and gradually decrease with time goes. While the reconstruction errors of Chi-2 HRRSs show an opposite trends (temporally increase). As for different pressures, the present developed HRRS also performs well in reconstructing the HRR fields and the reconstruction errors are much smaller than those of the two previous HRRSs. As for different turbulent Reynolds numbers, the developed HRRS can also stably and accurately reconstruct the temporal HRR fields, as shown in Fig. 19(e). In summary, the present developed can well reconstruct the HRR fields under various conditions, and its performance is temporally stable and obviously superior to those of the two previous HRRSs.

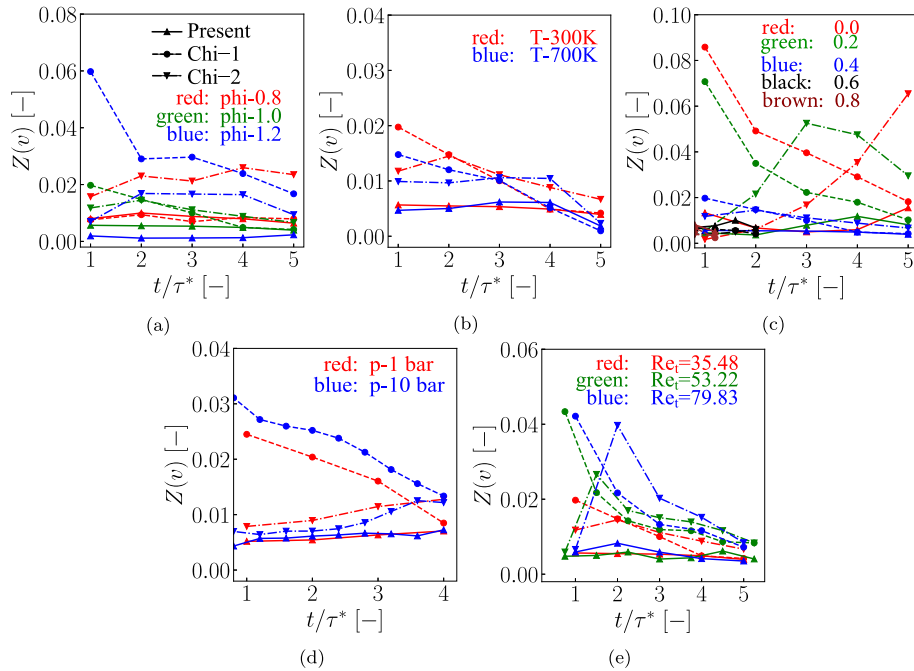


Fig. 19. Comparisons of temporal evolution of the reconstruction errors using the developed HRRS and two previous HRRSs under various conditions: (a) different equivalence ratios (0.8, 1.0, and 1.2); (b) different initial temperatures (300 and 700 K); (c) different BRs (0, 0.2, 0.4, 0.6, and 0.8); (d) different pressures (1 and 10 bar); (e) different turbulent Reynolds numbers ($Re_t = 35.48, 53.22, \text{ and } 79.83$).

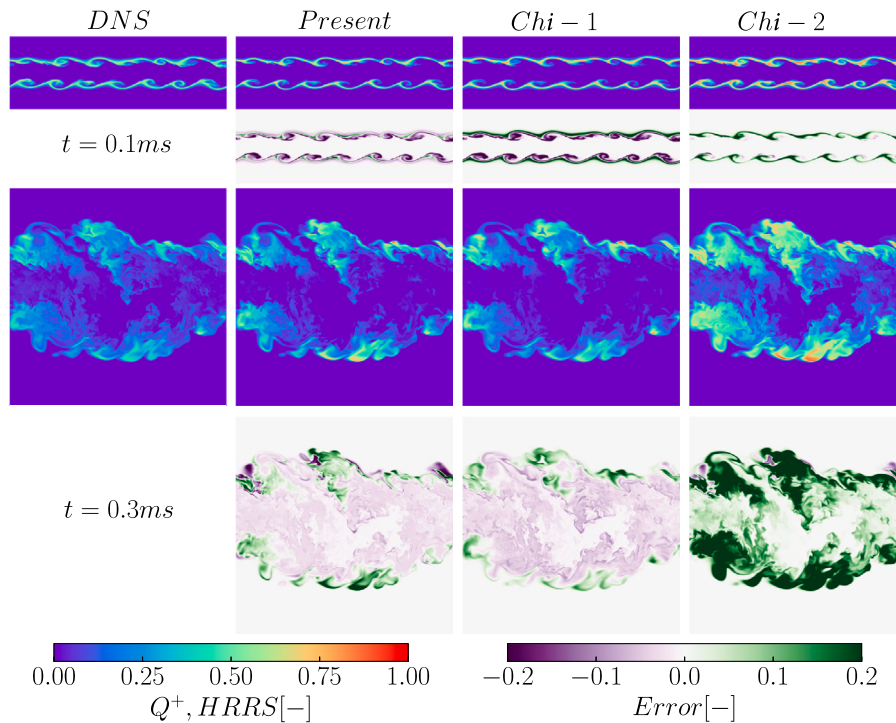


Fig. 20. Comparisons of the HRR fields obtained in the 3D-DNS and reconstructed using HRRSs at two time instants ($t = 0.1$ and 0.3 ms). The absolute errors are also plotted.

4.3.3. 3D temporally evolving planer jet flame

Fig. 20 shows comparisons of the HRR fields obtained from the 3D-DNS and reconstructed using the present developed HRRSs and two previous HRRSs at two time instants ($t = 0.1$ and 0.3 ms). For brevity, only cross-section plots along z direction are shown here. At $t = 0.1$ ms,

the development of jet flow is in a relatively early stage, and the vortex stretch in the third direction is not strong. Therefore, the HRR fields are similar as those in the 2D cases. For such a relatively early stage, Chi-2 HRRS performs slightly better, which is consistent with the results in 2D cases. The present developed HRRS can also give comparable HRR

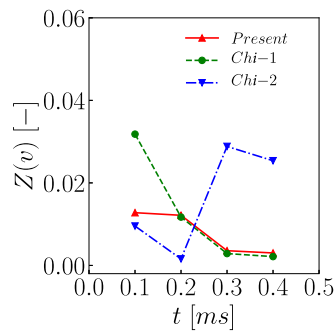


Fig. 21. Comparisons of temporal evolution of the reconstruction errors using the developed HRRS and two previous HRRSs in the 3D DNS.

reconstructions. The Chi-1 HRRS performs the worst. With the further development of the jet flow, the HRR structure becomes much more complicated. Specifically, there are continuous high HRR regions in the jet exterior, and some discontinuous structures of relatively low heat release rate generated by the fine turbulent vortex structures can be found in the jet interior. The present developed and Chi-1 HRRSs show an obviously better HRR reconstruction than that of Chi-2 HRRS. In particular, the high HRR fields in both the jet exterior and interior are significantly overestimated using Chi-2 HRRS.

Fig. 21 shows the temporal evolution of the reconstruction errors for the present developed HRRS and the two previous HRRSs. The temporal evolution shows a similar trend as that in the 2D cases: The reconstruction errors of the present developed HRRS is temporally more stable than the two previous HRRSs. Chi-1 performs worse in the early stage and the reconstruction error temporally decrease; Chi-2 performs well in the early stage but its performance temporally becomes worse. Overall, the validation results in the 3D premixed flame show that the present developed HRRS are more superior and stable than the two previous HRRSs.

5. Conclusions

In the present study, the existing reaction mechanisms were evaluated for hydrogen–ammonia premixed flame under various conditions by comparing with the experimental data. Series of 1D, 2D, and 3D laminar and turbulent premixed flames under various blending ratios, pre-heat temperatures, equivalence ratios, and pressures, were calculated to construct a flame database. A general HRRS for ammonia–hydrogen premixed flames under various conditions was identified from the database using a grid-search optimization method. The identified HRRS was further validated on the remaining 1D and 2D/3D-DNS data in a *posterior* manner, and compared with the previous HRRSs with the DNS data as benchmarks. The main findings and conclusions are listed as below:

- The evaluation of reaction kinetics indicates that the reaction mechanism developed by Shrestha et al. [10] has the best performance in predicting the laminar flame speeds for ammonia–hydrogen premixed flames under various conditions.
- The effects of equivalence ratio and blending ratio are significant in HRR reconstruction, especially for rich and high blending ratio conditions. While the effects of pressures and pre-heat temperature are relatively limited.
- A general HRRS, $[\text{NH}_2]^{1.53}[\text{OH}]^{0.28}$, is identified, which can accurately reconstruct the HRR field under various conditions. The *a posterior* validation on the remaining 1D and 2D/3D-DNS data and comparisons with the previous two HRRSs also demonstrate that the present developed HRRS is superior and more stable temporally.

Declaration of competing interest

The authors declare that they have no known competing financial interests or personal relationships that could have appeared to influence the work reported in this paper.

Data availability

Data will be made available on request.

Acknowledgments

The authors are grateful for the supports from Japan Society for the Promotion of Science (Grant No. : 21P20351). This work was partially supported by MEXT as “Program for Promoting Researches on the Supercomputer Fugaku” (Development of the Smart design system on the supercomputer “Fugaku” in the era of Society 5.0)(JP-MXP1020210316). This work used computational resources of the supercomputer Fugaku provided by RIKEN through the HPCI System Research Projects (Project ID: hp220141; hp220180).

References

- [1] Kobayashi H, Hayakawa A, Somaratne KKA, Okafor EC. Science and technology of ammonia combustion. *Proc Combust Inst* 2019;37(1):109–33.
- [2] An Z, Xing J, Kurose R. Numerical study on the phase change and spray characteristics of liquid ammonia flash spray. *Fuel* 2023;345:128229.
- [3] Hayakawa A, Arakawa Y, Mimoto R, Somaratne KKA, Kudo T, Kobayashi H. Experimental investigation of stabilization and emission characteristics of ammonia/air premixed flames in a swirl combustor. *Int J Hydrogen Energy* 2017;42(19):14010–8.
- [4] Wiseman S, Rieth M, Gruber A, Dawson JR, Chen JH. A comparison of the blow-out behavior of turbulent premixed ammonia/hydrogen/nitrogen-air and methane–air flames. *Proc Combust Inst* 2021;38(2):2869–76.
- [5] Rieth M, Gruber A, Williams FA, Chen JH. Enhanced burning rates in hydrogen-enriched turbulent premixed flames by diffusion of molecular and atomic hydrogen. *Combust Flame* 2022;239:111740.
- [6] Zhang M, An Z, Wang L, Wei X, Jianayihan B, Wang J, et al. The regulation effect of methane and hydrogen on the emission characteristics of ammonia/air combustion in a model combustor. *Int J Hydrogen Energy* 2021;46(40):21013–25.
- [7] Honzawa T, Kai R, Okada A, Valera-Medina A, Bowen PJ, Kurose R. Predictions of NO and CO emissions in ammonia/methane/air combustion by LES using a non-adiabatic flamelet generated manifold. *Energy* 2019;186:115771.
- [8] Li J, Huang H, Kobayashi N, He Z, Osaka Y, Zeng T. Numerical study on effect of oxygen content in combustion air on ammonia combustion. *Energy* 2015;93:2053–68.
- [9] Mei B, Zhang X, Ma S, Cui M, Guo H, Cao Z, et al. Experimental and kinetic modeling investigation on the laminar flame propagation of ammonia under oxygen enrichment and elevated pressure conditions. *Combust Flame* 2019;210:236–46.
- [10] Shrestha KP, Lhuillier C, Barbosa AA, Brequigny P, Contino F, Mounaïm-Rousselle C, et al. An experimental and modeling study of ammonia with enriched oxygen content and ammonia/hydrogen laminar flame speed at elevated pressure and temperature. *Proc Combust Inst* 2021;38(2):2163–74.
- [11] Wang S, Elbaz AM, Wang Z, Roberts WL. The effect of oxygen content on the turbulent flame speed of ammonia/oxygen/nitrogen expanding flames under elevated pressures. *Combust Flame* 2021;232:111521.
- [12] Okafor EC, Kurata O, Yamashita H, Inoue T, Tsujimura T, Iki N, et al. Liquid ammonia spray combustion in two-stage micro gas turbine combustors at 0.25 MPa; relevance of combustion enhancement to flame stability and NOx control. *Appl Energy Combust Sci* 2021;7:100038.
- [13] Chen Y, Zhang B, Su Y, Sui C, Zhang J. Effect and mechanism of combustion enhancement and emission reduction for non-premixed pure ammonia combustion based on fuel preheating. *Fuel* 2022;308:122017.
- [14] Yin Y, Gong X, Zhou H, Ren Z. The correlation of species concentration with heat release rate in an auto-igniting turbulent n-heptane spray flame. *Fuel* 2020;262:116510.
- [15] Eckbreth AC. *Laser diagnostics for combustion temperature and species*, vol. 3. CRC Press; 1996.
- [16] Najm HN, Paul PH, Mueller CJ, Wyckoff PS. On the adequacy of certain experimental observables as measurements of flame burning rate. *Combust Flame* 1998;113(3):312–32.
- [17] Karan A, Dayma G, Chauveau C, Halter F. Insight into the inner structure of stretched premixed ammonia-air flames. *Proc Combust Inst* 2023;39(2):1743–52.

- [18] Pugh D, Runyon J, Bowen P, Giles A, Valera-Medina A, Marsh R, et al. An investigation of ammonia primary flame combustor concepts for emissions reduction with OH*, NH₂* and NH* chemiluminescence at elevated conditions. *Proc Combust Inst* 2021;38(4):6451–9.
- [19] Chi C, Janiga G, Zähringer K, Thévenin D. DNS study of the optimal heat release rate marker in premixed methane flames. *Proc Combust Inst* 2019;37(2):2363–71.
- [20] Nikolaou ZM, Swaminathan N. Heat release rate markers for premixed combustion. *Combust Flame* 2014;161(12):3073–84.
- [21] Zhou T, Tang P, Ye T. Machine learning based heat release rate indicator of premixed methane/air flame under wide range of equivalence ratio. *Energy* 2023;263:126103.
- [22] Ayoola B, Balachandran R, Frank J, Mastorakos E, Kaminski C. Spatially resolved heat release rate measurements in turbulent premixed flames. *Combust Flame* 2006;144(1–2):1–16.
- [23] Chi C, Janiga G, Abdelsamie A, Zähringer K, Turányi T, Thévenin D. DNS study of the optimal chemical markers for heat release in syngas flames. *Flow Turbul Combust* 2017;98:1117–32.
- [24] Marshall GJ, Pitz RW. Evaluation of heat release indicators in lean premixed H₂/Air cellular tubular flames. *Proc Combust Inst* 2019;37(2):2029–36.
- [25] Gazi A, Vourliotakis G, Skevis G, Founti MA. Assessment of chemical markers for heat-release rate correlations in laminar premixed flames. *Combust Sci Technol* 2013;185(10):1482–508.
- [26] Cheng M, Wang H, Xiao H, Luo K, Fan J. Emission characteristics and heat release rate surrogates for ammonia premixed laminar flames. *Int J Hydrogen Energy* 2021;46(24):13461–70.
- [27] Song C, Wang H, Cheng M, Tian T, Luo K, Fan J. A DNS study of heat release rate surrogates with unity and non-unity exponents for ammonia/air premixed flames. *Int J Hydrogen Energy* 2023.
- [28] Zhu X, Guiberti TF, Li R, Roberts WL. Numerical study of heat release rate markers in laminar premixed ammonia-methane-air flames. *Fuel* 2022;318:123599.
- [29] Chi C, Sreekumar S, Thévenin D. Data-driven discovery of heat release rate markers for premixed NH₃/H₂/air flames using physics-informed machine learning. *Fuel* 2022;330:125508.
- [30] Yang W, Dinesh KR, Luo K, Thevenin D. Direct numerical simulation of turbulent premixed ammonia and ammonia-hydrogen combustion under engine-relevant conditions. *Int J Hydrogen Energy* 2022;47(20):11083–100.
- [31] Han X, Wang Z, Costa M, Sun Z, He Y, Cen K. Experimental and kinetic modeling study of laminar burning velocities of NH₃/air, NH₃/H₂/air, NH₃/CO/air and NH₃/CH₄/air premixed flames. *Combust Flame* 2019;206:214–26.
- [32] Ichikawa A, Hayakawa A, Kitagawa Y, Somarathne KKA, Kudo T, Kobayashi H. Laminar burning velocity and Markstein length of ammonia/hydrogen/air premixed flames at elevated pressures. *Int J Hydrogen Energy* 2015;40(30):9570–8.
- [33] Kumar P, Meyer TR. Experimental and modeling study of chemical-kinetics mechanisms for H₂-NH₃-air mixtures in laminar premixed jet flames. *Fuel* 2013;108:166–76.
- [34] Lee J, Kim J, Park J, Kwon O. Studies on properties of laminar premixed hydrogen-added ammonia/air flames for hydrogen production. *Int J Hydrog Energy* 2010;35(3):1054–64.
- [35] Li J, Huang H, Kobayashi N, He Z, Nagai Y. Study on using hydrogen and ammonia as fuels: Combustion characteristics and NO_x formation. *Int J Energy Res* 2014;38(9):1214–23.
- [36] Dagaut P, Glarborg P, Alzueta MU. The oxidation of hydrogen cyanide and related chemistry. *Prog Energy Combust Sci* 2008;34(1):1–46.
- [37] Klippenstein SJ, Pfeifle M, Jasper AW, Glarborg P. Theory and modeling of relevance to prompt-NO formation at high pressure. *Combust Flame* 2018;195:3–17.
- [38] Konnov A. Implementation of the NCN pathway of prompt-NO formation in the detailed reaction mechanism. *Combust Flame* 2009;156(11):2093–105.
- [39] Mathieu O, Petersen EL. Experimental and modeling study on the high-temperature oxidation of ammonia and related NO_x chemistry. *Combust Flame* 2015;162(3):554–70.
- [40] Nakamura H, Hasegawa S, Tezuka T. Kinetic modeling of ammonia/air weak flames in a micro flow reactor with a controlled temperature profile. *Combust Flame* 2017;185:16–27.
- [41] Okafor EC, Naito Y, Colson S, Ichikawa A, Kudo T, Hayakawa A, et al. Measurement and modelling of the laminar burning velocity of methane-ammonia-air flames at high pressures using a reduced reaction mechanism. *Combust Flame* 2019;204:162–75.
- [42] Otomo J, Koshi M, Mitsumori T, Iwasaki H, Yamada K. Chemical kinetic modeling of ammonia oxidation with improved reaction mechanism for ammonia/air and ammonia/hydrogen/air combustion. *Int J Hydrogen Energy* 2018;43(5):3004–14.
- [43] Shrestha KP, Seidel L, Zeuch T, Mauss F. Detailed kinetic mechanism for the oxidation of ammonia including the formation and reduction of nitrogen oxides. *Energy Fuels* 2018;32(10):10202–17.
- [44] Stagni A, Cavallotti C, Arunthanayothin S, Song Y, Herbinet O, Battin-Leclerc F, et al. An experimental, theoretical and kinetic-modeling study of the gas-phase oxidation of ammonia. *React Chem Eng* 2020;5(4):696–711.
- [45] Zhang K, Li Y, Yuan T, Cai J, Glarborg P, Qi F. An experimental and kinetic modeling study of premixed nitromethane flames at low pressure. *Proc Combust Inst* 2011;33(1):407–14.
- [46] Goodwin DG, Moffat HK, Schoegl I, Speth RL, Weber BW. Cantera: An object-oriented software toolkit for chemical kinetics, thermodynamics, and transport processes. 2022. <http://dx.doi.org/10.5281/zenodo.6387882>, Version 2.6.0, <https://www.cantera.org>.
- [47] Xiao H, Valera-Medina A, Bowen PJ. Modeling combustion of ammonia/hydrogen fuel blends under gas turbine conditions. *Energy Fuels* 2017;31(8):8631–42.
- [48] An Z, Zhang M, Zhang W, Xing J, Kurose R. Combustion characteristic of swirl flames using on-line cracking of ammonia to replace methane in a model gas turbine. In: The 60th Japanese combustion symposium. 2022.
- [49] Xing J, Luo K, Wang H, Jin T, Cai R, Fan J. A DNS study on temporally evolving jet flames of pulverized coal/biomass co-firing with different blending ratios. *Proc Combust Inst* 2021;38(3):4005–12.
- [50] Xing J, Luo K, Kurose R, Fan J. An extended flamelet/progress variable model for coal/biomass co-firing flame. *Proc Combust Inst* 2022.
- [51] Jasak H, Jemcov A, Tukovic Z, et al. Openfoam: A c++ library for complex physics simulations. In: International workshop on coupled methods in numerical dynamics, vol. 1000. 2007, p. 1–20.
- [52] Xing J, Luo K, Wang H, Gao Z, Jin T, Fan J. Comparative study on different treatments of coal devolatilization for pulverized coal combustion simulation. *Energy Fuels* 2020;34(3):3816–27.
- [53] Zhao C, Luo K, Cai R, Xing J, Gao Z, Fan J. Large eddy simulations and analysis of NO emission characteristics in a laboratory pulverized coal flame. *Fuel* 2020;279:118316.
- [54] Luo K, Zhao C, Wen X, Gao Z, Bai Y, Xing J, et al. A priori study of an extended flamelet/progress variable model for NO prediction in pulverized coal flames. *Energy* 2019;175:768–80.
- [55] Dasgupta A, Gonzalez-Juez E, Haworth DC. Flame simulations with an open-source code. *Comput Phys Comm* 2019;237:219–29.
- [56] Jin T, Wu Y, Wang X, Luo KH, Lu T, Luo K, et al. Ignition dynamics of DME/methane-air reactive mixing layer under reactivity controlled compression ignition conditions: Effects of cool flames. *Appl Energy* 2019;249:343–54.
- [57] Göktolga MU, van Oijen JA, de Goey LPH. 3D DNS of MILD combustion: a detailed analysis of heat loss effects, preferential diffusion, and flame formation mechanisms. *Fuel* 2015;159:784–95.
- [58] Kai R, Tokuoaka T, Nagao J, Pillai AL, Kurose R. LES flamelet modeling of hydrogen combustion considering preferential diffusion effect. *Int J Hydrogen Energy* 2023;48(29):11086–101.
- [59] Tang H, Ezendevea D, Magnotti G. Simultaneous measurements of NH₂ and major species and temperature with a novel excitation scheme in ammonia combustion at atmospheric pressure. *Combust Flame* 2023;250:112639.
- [60] Fan Q, Liu X, Cai X, Brackmann C, Alden M, Bai X-S, et al. Structure and scalar correlation of ammonia/air turbulent premixed flames in the distributed reaction zone regime. *Combust Flame* 2022;241:112090.